Supplemental Document

Free-electron-driven X-ray caustics from strained van der Waals materials: supplement

XIHANG SHI,[1] MICHAEL SHENTCIS,[1] YANIV KURMAN,[1] LIANG JIE WONG,[2] F. JAVIER GARCÍA DE ABAJO,[3,4] AND IDO KAMINER[1,*]

[1] *Solid State Institute and Faculty of Electrical and Computer Engineering, Technion – Israel Institute of Technology, 32000 Haifa, Israel*
[2] *School of Electrical and Electronic Engineering, Nanyang Technological University, Singapore 639798, Singapore*
[3] *ICFO–Institut de Ciencies Fotoniques, The Barcelona Institute of Science and Technology, Castelldefels, Spain*
[4] *ICREA–Institució Catalana de Recerca i Estudis Avançats, Passeig Lluís Companys 23, 08010 Barcelona, Spain*
[*] *Corresponding author:* kaminer@technion.ac.il

Supplement DOI: https://doi.org/10.6084/m9.figshare.21908631

Parent Article DOI: https://doi.org/10.1364/OPTICA.472462

Supplementary Material of Free-electron-driven X-ray caustics from strained van der Waals materials

XIHANG SHI[1], MICHAEL SHENTCIS[1], YANIV KURMAN[1], LIANG JIE WONG[2], F. JAVIER GARCÍA DE ABAJO[3,4] AND IDO KAMINER[1†]

[1]Solid State Institute and Faculty of Electrical and Computer Engineering, Technion – Israel Institute of Technology, 32000 Haifa, Israel
[2]School of Electrical and Electronic Engineering, Nanyang Technological University, Singapore, Singapore
[3]ICFO–Institut de Ciencies Fotoniques, The Barcelona Institute of Science and Technology, Castelldefels, Spain
[4]ICREA–Institució Catalana de Recerca i Estudis Avançats, Passeig Lluís Companys 23, 08010 Barcelona, Spain
[†] Corresponding Author: kaminer@technion.ac.il

Contents

Section 1 | The scattering field of a free electron by a 2D crystal layer

When a free electron traverses a 2D crystal layer with Bravais lattice spanning the x - y plane at $z = 0$, the electromagnetic field that accompanies the free electron is scattered by a collection of atoms modeled as a dipole array characterized by their linear atomic polarizability. To exploit the discrete translational symmetry of the lattice, we use the 2D Fourier transform [1] of a function $f(\mathbf{R})$ located at the lattice sites $\mathbf{r}_n = (\mathbf{R}_n,0)$, $f_n = f(\mathbf{r}_n)$, defined as

$$\begin{aligned} f(\mathbf{Q}) &= A\sum_{n=1}^{\infty} e^{-i\mathbf{Q}\cdot\mathbf{R}_n} f_n \,, \\ f_n &= \int_{\mathrm{BZ}} \frac{d^2\mathbf{Q}}{(2\pi)^2} e^{i\mathbf{Q}\cdot\mathbf{R}_n} f(\mathbf{Q}) \,, \end{aligned} \tag{1}$$

where A is the area of the lattice unit cell and BZ indicates that the integral over $\mathbf{Q}$ is performed within the first Brillouin zone (BZ) of the reciprocal lattice.

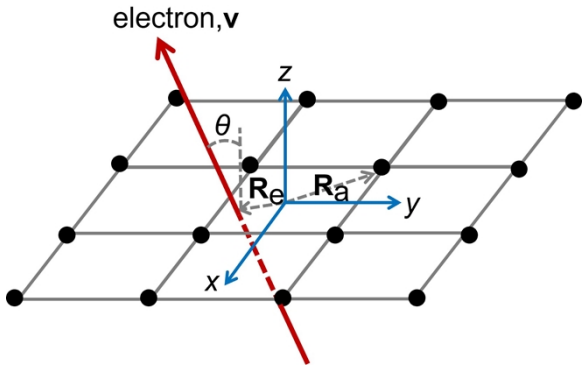

Fig. s1. Schematic of a free electron traversing a 2D crystal layer spanning the $x-y$ plane at $z = 0$. The electron velocity forms an incidence angle θ with respect to the crystal layer normal. $\mathbf{R}_\mathrm{a}$ and $\mathbf{R}_\mathrm{e}$ denote the in-plane distances from the center of the unit cell to the atom and electron crossing position, respectively.

The free electron is described as a classical point charge in $\mathbf{r}$-t space, introducing its current density $\mathbf{J}(\mathbf{r},t) = -e\mathbf{v}\delta(\mathbf{r} - \mathbf{r}_\mathrm{e} - \mathbf{v}t)$, where $\mathbf{r}_\mathrm{e}=(\mathbf{R}_\mathrm{e},0)$ denotes the displacement of the electron in the z=0 plane at time t=0, $-e$ is the electron charge, and $\mathbf{v}$ is the electron velocity vector. The current density in $\mathbf{q}$-ω space is $\mathbf{J}(\mathbf{q},\omega) = -2\pi e\mathbf{v}e^{-i\mathbf{q}\cdot\mathbf{R}_\mathrm{e}}\delta(\omega - \mathbf{q}\cdot\mathbf{v})$. The electromagnetic field that accompanies the free electron is then [2]

$$\begin{aligned} \mathbf{E}^{\mathrm{inc}}(\mathbf{r},\omega) &= 2i\pi\omega\mu_0 e\int \frac{d^3\mathbf{q}}{(2\pi)^3}\left(\bar{\bar{\mathrm{I}}} - \frac{\mathbf{q}\mathbf{q}}{k^2}\right)\frac{e^{i\mathbf{q}\cdot(\mathbf{r}-\mathbf{r}_\mathrm{e})}}{k^2-q^2}\cdot\mathbf{v}\delta(\omega-\mathbf{q}\cdot\mathbf{v}) \\ &= \frac{ie}{\varepsilon_0 v_z}\int \frac{d^2\mathbf{Q}}{(2\pi)^2}\frac{k\,\mathbf{v}/c - \mathbf{q}}{k^2-q^2}e^{i\mathbf{q}\cdot(\mathbf{r}-\mathbf{r}_\mathrm{e})} \\ &= \int \frac{d^2\mathbf{Q}}{(2\pi)^2}\mathbf{E}^{\mathrm{inc}}(\mathbf{Q},\omega)e^{i\mathbf{Q}\cdot\mathbf{R}} \,, \end{aligned} \tag{2}$$

where ω and $k = \omega/c$ are the photon angular frequency and wavenumber, μ_0 and ε_0 are the vacuum permeability and permittivity, $\mathbf{Q}$ is the x - y component of the Fourier wave vector $\mathbf{q} = \left(\mathbf{Q}, \frac{\omega - \mathbf{Q}\cdot\mathbf{v}_\parallel}{v_z}\right)$ (notice that the z component is determined by the δ function in Eq. (2)), $\mathbf{R}$ is the x - y component of the position vector, and $\mathbf{E}^{\mathrm{inc}}(\mathbf{Q},\omega)$ is the 2D Fourier transform of $\mathbf{E}^{\mathrm{inc}}(\mathbf{r},\omega)$.

The atomic dipole moment at position $\mathbf{r}_\mathrm{d} = (\mathbf{R}_n + \mathbf{R}_\mathrm{a},0)$ is denoted as $\mathbf{p}_n = \alpha(\omega)\mathbf{E}^\mathrm{inc}(\mathbf{r}_\mathrm{d},\omega)$, where $\mathbf{R}_n$ is the 2D lattice site position, $\mathbf{R}_\mathrm{a}$ is the position of the atom relative to the center of the unit cell, and $\alpha(\omega)$ is the atomic polarizability that can be derived from the scattering factor [3]. The field scattered by the 2D dipole array is

$$\mathbf{E}^\mathrm{sca}(\mathbf{r},\omega) = \omega^2\mu_0 \sum_n \bar{\bar{\mathrm{G}}}(\mathbf{r}-\mathbf{r}_\mathrm{d}) \cdot \mathbf{p}_n(\omega)\,, \tag{3}$$

where $\bar{\bar{\mathrm{G}}}(\mathbf{r}-\mathbf{r}_\mathrm{d})$ is the electromagnetic dyadic Green function. The latter can be expanded as $\bar{\bar{\mathrm{G}}}(\mathbf{r}-\mathbf{r}_\mathrm{d}) = \frac{i}{2k^2}$ $\int \frac{d^2\mathbf{Q}}{(2\pi)^2}\frac{k^2-\mathbf{kk}}{k_z}e^{i\,\mathbf{Q}\cdot(\mathbf{R}-\mathbf{R}_n-\mathbf{R}_\mathrm{a})+ik_z|z|}$, where $\mathbf{k} = (\mathbf{Q},\ \pm k_z)$ and $k_z = \sqrt{k^2-Q^2}$. The atomic dipole moment $\mathbf{p}_n(\omega)$ is also Fourier expanded following Eq. (1) as $\mathbf{p}_n(\omega) = \int_\mathrm{BZ} \frac{d^2\mathbf{Q}}{(2\pi)^2}e^{i\mathbf{Q}\cdot\mathbf{R}_n}\mathbf{p}(\mathbf{Q},\omega)$. By making use of the identity $\sum_n e^{i\mathbf{Q}\cdot\mathbf{R}_n} = \sum_\mathbf{G} \frac{(2\pi)^2}{A}\delta(\mathbf{Q}-\mathbf{G})$, where $\mathbf{G}$ is the 2D reciprocal lattice vector and A is the area to a 2D unit cell, the electron scattering field in Eq. (3) becomes

$$\mathbf{E}^\mathrm{sca}(\mathbf{r},\omega) = \frac{i}{2A\varepsilon_0}\int \frac{d^2\mathbf{Q}}{(2\pi)^2}\frac{k^2-\mathbf{kk}}{k_z}\cdot\mathbf{p}(\mathbf{Q},\omega)e^{i\mathbf{Q}\cdot(\mathbf{R}-\mathbf{R}_\mathrm{a})+ik_z|z|}\,. \tag{4}$$

It should be noted that $\mathbf{Q}$ is not limited to the first BZ and is periodic in reciprocal lattice space, and the identity $\mathbf{p}(\mathbf{Q},\omega) = \mathbf{p}(\mathbf{Q}+\mathbf{G},\omega)$ follows from the definition in Eq. (1). Under the assumption of isotropic polarizabilities, the dipole moment $\mathbf{p}_n(\omega)$ is linearly polarized along the direction of the electron electric field at position $\mathbf{r}=(\mathbf{R}_n,0)$. We also note that the linear polarizability is $\alpha(\omega)/(\varepsilon_0 V_\mathrm{cell}) \ll 1$ (of the same order as the susceptibility) in the X-ray range, where V_cell is the volume of one unit cell (i.e., the 2D unit cell area A times the interlayer spacing). The dipole-dipole interaction is neglected as it is of order $O(\alpha^2)$, and therefore, we have

$$\begin{aligned}\mathbf{p}_n(\omega) &= \alpha(\omega)\mathbf{E}^\mathrm{inc}(\mathbf{r}_\mathrm{d},\omega),\\ \mathbf{p}(\mathbf{Q},\omega) &= \alpha(\omega)\sum_\mathbf{G}\mathbf{E}^\mathrm{inc}(\mathbf{Q}+\mathbf{G},\omega)\,e^{i(\mathbf{Q}+\mathbf{G})\cdot\mathbf{R}_\mathrm{a}}\,,\end{aligned} \tag{5}$$

where the second equation is the Fourier transform of the first one, and $\mathbf{E}^\mathrm{inc}(\mathbf{Q}+\mathbf{G},\omega)$ is the 2D Fourier transform of $\mathbf{E}^\mathrm{inc}(\mathbf{r},\omega)$ defined in Eq. (2). Combining Eqs. (2), (4), and (5), we have

$$\begin{aligned}\mathbf{E}^\mathrm{sca}(\mathbf{r},\omega) &= \frac{i\alpha(\omega)}{2A\varepsilon_0}\sum_\mathbf{G}\int\frac{d^2\mathbf{Q}}{(2\pi)^2}\frac{k^2-\mathbf{kk}}{k_z}\cdot\mathbf{E}^\mathrm{inc}(\mathbf{Q}+\mathbf{G},\omega)e^{i\mathbf{Q}\cdot\mathbf{R}+i\mathbf{G}\cdot\mathbf{R}_\mathrm{a}+ik_z|z|}\\ &= -\frac{\alpha(\omega)e}{2Av_z\varepsilon_0^2}\sum_\mathbf{G}\int\frac{d^2\mathbf{Q}}{(2\pi)^2}\frac{k^2-\mathbf{kk}}{k_z}\cdot\frac{k\,\mathbf{v}/c-\mathbf{Q}_\mathbf{G}-q_z\hat{z}}{k^2-\mathbf{Q}_\mathbf{G}^2-q_z^2}e^{i\mathbf{G}\cdot(\mathbf{R}_\mathrm{a}-\mathbf{R}_\mathrm{e})+i\mathbf{Q}\cdot(\mathbf{R}-\mathbf{R}_\mathrm{e})+ik_z|z|}\,,\end{aligned} \tag{6}$$

where $k_z = \sqrt{k^2-Q^2}$, $\mathbf{Q}_\mathbf{G} = \mathbf{Q}+\mathbf{G}$ and $q_z = \frac{\omega-\mathbf{Q}_\mathbf{G}\cdot\mathbf{v}}{v_z}$. Using the saddle-point approach and the Weyl identity $\frac{e^{ikr}}{r} = \frac{i}{2\pi}\int d^2\mathbf{Q}\frac{e^{i(k_x x+k_y y+k_z|z|)}}{k_z}$, we arrive at the following analytical expression for the scattering field produced by a free electron upon interaction with the atomic array:

$$\mathbf{E}^\mathrm{sca}(\mathbf{G},\mathbf{r},\omega) = \frac{ie\alpha(\omega)}{Av_z\varepsilon_0^2}(k^2-\mathbf{kk})\cdot\frac{k\,\mathbf{v}/c-\mathbf{Q}_\mathbf{G}-q_z\hat{z}}{k^2-\mathbf{Q}_\mathbf{G}{}^2-q_z^2}\frac{e^{ikr'+i\mathbf{G}\cdot(\mathbf{R}_\mathrm{a}-\mathbf{R}_\mathrm{e})}}{4\pi r'}, \tag{7}$$

where $r' = |\mathbf{r}-\mathbf{r}_\mathrm{e}|$ is the far-field distance from the point where the electron transverses the 2D layer.

It should be noted that the saddle-point approach in deriving Eq. (7) uses the far-field approximation. This is reasonable considering the sub-nanometer to nanometer wavelength of X-rays. However, caustics are not in the far zone of the material as a whole. On the contrary, it is in the prewave zone [4], where the size of the source is significant to the caustics. In order to incorporate the finite size and geometry of the source (along the electron trajectory) in the simulation, we sum up the radiation scattered by each layer fixed at different positions.

Section 2 | The dispersion of PXR emission from a bent crystal

We substitute the bent multilayers by a series of flat layers of different orientations relative to each other. Their positions and normal vectors are determined to match those of the bent vdW structure at the points, for example point S in Fig.s2, where the electron crosses the corresponding bent layers. We sketch in Fig. s2 how a bent layer (blue curve) can be substituted by a flat layer (dashed red line). We can image the bent layer being flattened around the point S without shearing deformation, and thus, the atomic positions around point S are the same in both layers. We consider that the crystal structure is cylindrically bent with mirror and translational symmetry along the radial line AC, so that the atom positions along such line remain invariant during the bending process. The point C on the bent layer is projected onto the point C' on the flat layer with the same in-plane distance to the tangential point S, such that $\overline{SC'} = \overset{\frown}{SC}$. From Eq. (7), we know that when the 2D Bravais lattice sits in the $z = 0$ plane and the electron passes through the 2D lattice at the origin point, the phase of the scattered field is $\phi = kr + \mathbf{G} \cdot \mathbf{R}_\mathrm{a}$. However, when the free electron passes through the equivalent flat layer in Fig. s2, the phase equation should be modified to include the changes of the electron impacting position and the atomic position $\mathbf{R}_\mathrm{a}$.

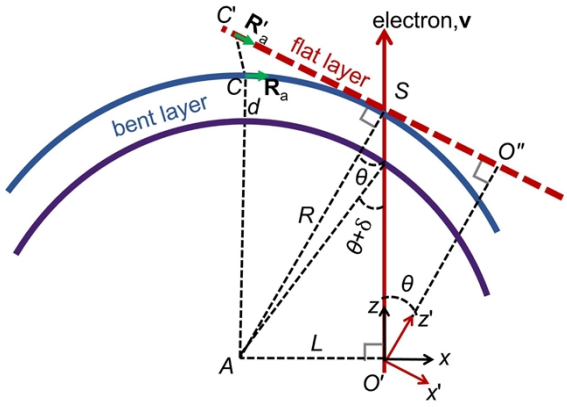

Fig. s2. Substituting flat layers for bent layers. The atomic positions along the line AC remain fixed during the bending process. A free electron (red arrow) traverses a bent layer (blue curve) at point S. The electron trajectory and the radial line AC are parallel and separated by a distance L. The blue bent layer is substituted by a flat layer (dashed red line) with the tangential point S. We introduce two frames: the x-z frame, in which the electron moves along the z-axis, and the x'-z' frame, in which the z' axis is perpendicular to the flat layer located at z'=$R\cos^2\theta$. Here, R is the radius of the bent layer and θ is the electron incidence angle relative to the normal direction (shared by the flat layer and the curved one to which is substitutes).

Vectors and their components in the $x-y$ ($x'-y'$) frame are denoted without (with) prime. We repeat the scattered field calculation from Eqs. (1) to (6) in the $x'-z'$ frame with the 2D flat layer located at $z' = R\cos^2\theta$ and the electron passing by point O' at time $t = 0$. The phase factor in the equation is thus $e^{i\mathbf{G}'\cdot\mathbf{R}'_\mathrm{a}+i\mathbf{Q}'\cdot\mathbf{R}'+ik_z|z-R\cos^2\theta|+iq'_zR\cos^2\theta}$,

where $q'_z = \left[\omega - (\mathbf{Q}' + \mathbf{G}') \cdot \mathbf{v}'_{\parallel}\right] / v'_z$, $\mathbf{v}'_{\parallel}$ and v'_z are the electron velocity components in the $x' - z'$ frame, $\mathbf{v} = -v\sin\theta\,\hat{x}' + v\cos\theta\hat{z}'$, and $\mathbf{R}'_{\mathrm{a}}$ is the atomic relative position in the $x' - y'$ frame.

We need to define $\mathbf{R}'_{\mathrm{a}}$ in a way such that it maintains the match of the atomic positions between the bent layer and the flat layer around the tangent point S. The in-plane atomic position of the bent layer $\mathbf{R}_{\mathrm{a}} = \sigma_1\hat{x} + \sigma_2\hat{y}$ relative to the line AC is marked by the green arrow. Correspondingly, $\mathbf{R}'_{\mathrm{a}}$ in the flat layer is defined relative to the point C' with $|\mathbf{R}_{\mathrm{a}}| = |\mathbf{R}'_{\mathrm{a}}|$ under the condition of plastic bending. In the $x' - z'$ frame, $\mathbf{R}'_{\mathrm{a}} = \sigma_1\hat{x}' + \sigma_2\hat{y}' - C'O'\hat{x}' = \sigma_1\hat{x}' + \sigma_2\hat{y}' - (R\theta + R\cos\theta\sin\theta)\hat{x}'$ with the 2D origin point at O''.

Consequently, the phase of the waves in the $x' - y'$ frame becomes $e^{i\mathbf{G}'\cdot(\sigma_1\hat{x}'+\sigma_2\hat{y}')-iG'_xR\theta+i\mathbf{Q}'\cdot(\mathbf{R}'+R\cos\theta\sin\theta\,\hat{x}')+ik_z|z'-R\cos^2\theta|+i\frac{\omega}{v}R\cos\theta}$. We use the saddle point approach to derive the far-field phase, that is, $\phi(\theta) = \mathbf{G}' \cdot \left(\sigma_1\hat{x}' + \sigma_2\hat{y}'\right) - G'_xR\theta + \frac{\omega}{v}R\cos\theta + k|\mathbf{r} - R\cos\theta\,\hat{z}|$. It should be noted that we have $\mathbf{G}' \cdot \left(\sigma_1\hat{x}' + \sigma_2\hat{y}'\right) = \mathbf{G} \cdot (\sigma_1\hat{x} + \sigma_2\hat{y})$ under the condition of plastic bending.

The relation between the incidence angle θ, its variation δ in the neighboring layer, and the interlayer distance d is $d = \frac{L}{\sin\theta} - \frac{L}{\sin(\theta+\delta)} \simeq L\frac{\cos\theta}{\sin^2\theta}\delta$. The radius is related to the incidence angle θ through $R\sin\theta = L$. The dispersion of radiation from the bent layers is obtained from $\phi(\theta + \delta) - \phi(\theta) = 2n\pi$, where n is an integer. This leads to

$$k\frac{z - L\cot\theta}{|\mathbf{r} - L\cot\theta\,\hat{z}|} = -\frac{2n\pi}{d}\cos\theta + \frac{\omega}{v} + G'_x(\sin\theta - \theta\cos\theta), \tag{8}$$

which is Eq. (2) in the main text, with G'_x replaced by $g_{\parallel}$ and $\frac{2n\pi}{d}$ replaced by $g_{\perp}$.

Section 3 | The trajectory equation of the X-ray Airy beam

From ray optical theory, Eq. (8) shows the θ-dependent trajectory of the rays, as shown in Fig. 1b of the main text. The envelope equation of the rays can be obtained by combining Eq. (8) and its derivative, that is,

$$\begin{aligned} k\frac{z - L\cot\theta}{|\mathbf{r} - L\cot\theta\,\hat{z}|} &= -\frac{2n\pi}{d}\cos\theta + \frac{\omega}{v} + G'_x(\sin\theta - \theta\cos\theta), \\ k\frac{\partial}{\partial\theta}\frac{z - L\cot\theta}{|\mathbf{r} - L\cot\theta\,\hat{z}|} &= \frac{\partial}{\partial\theta}\left[-\frac{2n\pi}{d}\cos\theta + \frac{\omega}{v} + G'_x(\sin\theta - \theta\cos\theta)\right]. \end{aligned} \tag{9}$$

Indeed, combing these two equations, we obtain the envelope equation

$$|\mathbf{r} - L\cot\theta\,\hat{z}| = \frac{L}{-\frac{2n\pi c}{d\omega}\sin^3\theta}\left[1 - \left(\frac{2n\pi c}{\omega d}\cos\theta + \frac{c}{v}\right)^2\right], \tag{10}$$

where we set $G'_x = 0$ because our numerical results show that this component dominates over the contribution of all other in-plane reciprocal lattice vectors.

The radius of the central layer is R, as indicated in Fig. s2. We also consider here another layer with radius $R + t$. The respective electron incidence angles are θ_0 and $\theta_0 + \delta\theta$, with $\sin\theta_0 = L/R$ and $L\frac{\cos\theta_0}{\sin^2\theta_0}\delta\theta \cong t$ under the condition $t \ll R$. Performing a Taylor expansion on both sides of Eq. (10), we have

$$
\begin{aligned}
&|\mathbf{r} - L\cot\theta\,\hat{z}\,| \\
&= -\frac{L}{\frac{2n\pi c}{d\omega}}\frac{1}{\sin^3\theta_0}\left[1-\left(\frac{2n\pi c}{d\omega}\cos\theta_0+\frac{c}{v}\right)^2\right]+\frac{L}{-\frac{2n\pi c}{d\omega}}\frac{1}{\sin^2\theta_0} \\
&\left[\frac{4c^2n\pi(d\omega+2n\pi v\cos\theta_0)}{d^2\omega^2 v}-3\left(1-\left(\frac{c}{v}+\frac{2n\pi c\cos\theta_0}{d\omega}\right)^2\right)\frac{\cos\theta_0}{\sin^2\theta_0}\right]\delta\theta - L\left(\frac{2n\pi c}{d\omega}\cos\theta_0+\frac{c}{v}\right)\frac{\delta\theta}{\sin^2\theta_0} \\
&= -\frac{L}{\frac{2n\pi c}{d\omega}}\frac{1}{\sin^3\theta_0}\left[1-\left(\frac{2n\pi c}{d\omega}\cos\theta_0+\frac{c}{v}\right)^2\right]+\frac{1}{-\frac{2n\pi c}{d\omega}} \\
&\left[\frac{4c^2n\pi(d\omega+2n\pi v\cos\theta_0)}{d^2\omega^2 v\cos\theta_0}-3\left(1-\left(\frac{c}{v}+\frac{2n\pi c\cos\theta_0}{d\omega}\right)^2\right)\frac{1}{\sin^2\theta_0}\right]t-\left(\frac{2n\pi c}{d\omega}+\frac{c}{v\cos\theta_0}\right)t \\
&= -\frac{d\omega}{2n\pi c}\frac{R^3}{L^2}\sin^2\varphi_0+3\left(-\frac{\cos\varphi_0}{\cos\theta_0}+\frac{d\omega}{2n\pi c}\frac{\sin^2\varphi_0}{\sin^2\theta_0}\right)t
\end{aligned}
\tag{11}
$$

where $\cos\varphi_0=\frac{1}{\beta}+\frac{n\lambda}{d}\cos\theta_0$ and $\cos\theta_0=\sqrt{1-\left(\frac{L}{R}\right)^2}$. The first term following the last equality represents the focal distance of the Airy beam, while the second term stands for the caustic axial distribution.

Section 4 | Justifying the substitution of a bent layer by a flat layer

We use a flat crystal layer to substitute the bent crystal layer in our calculation. In what follows, we justify the approximation by comparing the phase difference of the electron excited dipoles on the flat layer and the bent layer within the Bohr cutoff range $L_{\mathrm{Bohr}}=v\gamma/\omega$, where $\gamma=1/\sqrt{1-v^2/c^2}$ is the Lorentz contraction factor. We note that L_{Bohr} measures the distance up to which the free electron field takes significant values (i.e., its spatial extension away from the electron trajectory). The Bohr cutoffs for (1) a 300 keV electron and 3 keV photon energy, (2) a 1 MeV electron and 3 keV photon energy, and (3) a 10 MeV electron and 10 keV photon energy are (1) 0.08 nm, (2) 0.18 nm, and (3) 0.40 nm, respectively.

The phase variation of the field supplied by a free electron moving along the z direction is $\omega z/v$. Therefore, the phase difference of the electron excited dipoles on two consecutive layers along the electron trajectory at the Bohr cutoff is $\frac{\omega}{v}\Delta h$, as shown in Fig. s3. We have $\Delta h=\frac{AB-R}{\cos\theta}$ by applying the approximation that OB is parallel to OA under the condition that $L_{\mathrm{Bohr}}\ll R$, since $AB-R=\frac{R}{\cos\alpha}-R=\frac{\alpha^2}{2}R$, $\Delta h=\frac{1}{2}\left(\frac{\frac{L_{\mathrm{Bohr}}}{\cos\theta}}{R}\right)^2\frac{R}{\cos\theta}=\frac{1}{2}\frac{L_{\mathrm{Bohr}}^2}{R\cos^3\theta}$. The phase difference is thus $\frac{\omega}{v}\Delta h=\frac{\beta\gamma^2\lambda}{4\pi R\cos^3\theta}$, where $\beta=\frac{v}{c}$. When the phase difference satisfies $\frac{\omega}{v}\Delta h\ll\frac{\pi}{2}$, the substitution is justifiable. In the main text, the kinetic energy of the electron is set to 1 MeV, the photon energy is 3 keV, the bending radius is $R=5$ μm, and the incidence angle is $\theta\simeq\sin^{-1}\left(\frac{4}{5}\right)$, and therefore, we have $\frac{\omega}{v}\Delta h\simeq 10^{-4}\ll 1$.

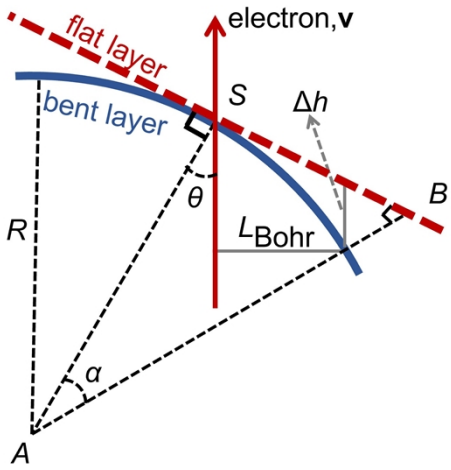

Fig. s3. Error produced by substituting a bent layer by a flat layer. The flat layer is tangential to the bent layer at point S, which is the electron impact point on the bent layer. The difference between the electron scattered fields in the two types of layers is estimated by discussing the phase difference of the dipoles on the two layers within the range of the electron Bohr cutoff ($L_{\mathrm{Bohr}}=v\gamma/\omega$), where v is the electron velocity, γ is the Lorentz factor, and ω is the angular frequency.

Section 5 | X-ray Airy beam from elastically bent vdW materials

We consider two crystal deformation mechanisms associated with bending in vdW materials: elastic and plastic bendings [5]. In the elastic bending regime, vdW multilayers are perfectly glued together and bend as a single plate, with a behavior that follows continuum mechanics plate theory. The latter is characterized by a length-invariant neutral surface, so that crystal layers are extended or compressed along the direction normal to such surface in proportion to the distance to it (Fig. s4). In the plastic bending mechanism, multilayer interfaces are ultralubricated, with each layer bending independently while locally maintaining in-plane atomic distances and interlayer separations nearly intact by shearing and slipping. Recent experimental results show that bending of vdW materials involves both types of mechanisms [6,7], although with a dominant contribution of the second one because the multilayers are held together by relatively weak vdW forces.

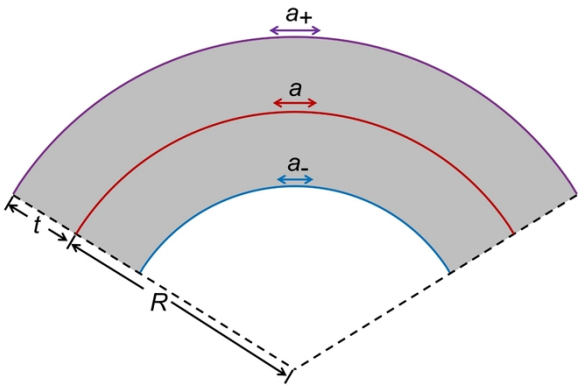

Fig. s4. Lattice variation of an elastic bending multilayer structure (cross section). The red curve is the length-invariant neutral surface, away from which the layers are extended (e.g., the purple curved surface) or

compressed (e.g., the blue curved surface) parallel to it by scales that are proportional to the distances from the neutral surface, and therefore, the magnitudes of in-plane reciprocal lattice vectors are inversely proportional to the radii.

We compare in Fig. s5 the X-ray Airy beam generated from a bent WSe2 multilayer structure modelled as elastic bending (Fig. s5a) or plastic bending (Fig. s5b). The numerical results show that there is no significant difference between the two results, as the specific Airy beam plotted in the image is mainly contributed by the zero $g_{||}$.

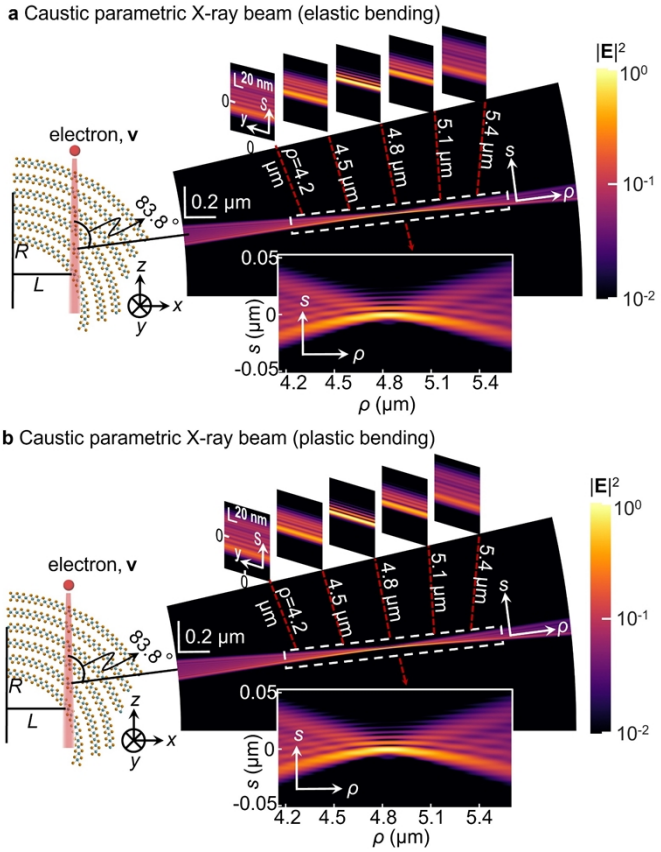

Fig. s5. Caustic X-ray beam from a cylindrically bent multilayer WSe2 heterostructure modelled in the elastic bending (a) and plastic bending (b) configurations. In the elastic bending model, the in-plane lattice constants are extended or compressed during the bending process, so the in-plane reciprocal lattices are correspondingly scaled down or up. In the plastic bending model, the in-plane lattice constants and reciprocal lattices remain invariant. The numerical results in both configurations are nearly identical because the caustic beam is mainly contributed by $g_{||} = 0$.

Section 6 | X-ray Airy beam formed by 15 keV photons

In the main text, we show the Airy beams of 3 keV photons excited by 1 MeV electrons. The focal lengths are of the order of microns. However, longer focal lengths can be pursued for application considerations. In Fig. s6, we show that focal lengths of millimeters to centimeters can be achieved by increasing the bending radius and sample thickness. The electron energy is set to be 10 MeV, as electrons with higher energy are less likely to diverge considering the space charge and electron scattering.

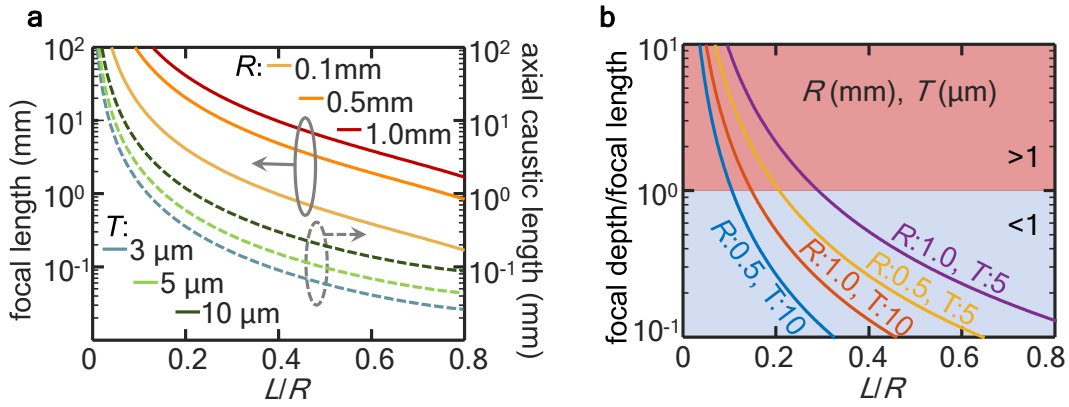

Fig. s6. Analysis of the generated X-ray Airy beam: quantifying its focal length, axial caustic length, and conditions for its formation. Panel (a) presents the focal length (left vertical axis) and axial caustic length (right vertical axis) as a function of the L/R ratio (see Fig. 2). The axial caustic length scales linearly with the thickness T (colored dashed curves), while the focal length changes when varying the bending radius R (colored solid curves), under the condition $T \ll R$. Panel (b) presents the regime in which an X-ray caustic can develop. Its formation is limited by wave diffraction, which sets a finite (nonzero) focal depth. The latter must be smaller than the focal length for a meaningful caustic to emerge. The ratio of focal depth to focal length is shown as the vertical axis. The regime in which caustics can (cannot) form is highlighted by a blue (red) background. The ratio is a function of bending radius R, thickness T, and L/R ratio. The electron kinetic energy is 10 MeV and the photon energy is 15 keV.

Section 7 | Electron beam divergence from space charge and electron scattering.

In this section, we analyze the electron beam divergence due to the effect of space charge and electron scattering inside the crystal.

The effect of space charge, i.e., the inter-electron repulsion, causes the electron beam divergence. It is much more significant for larger electron currents and smaller spot sizes. In general, the divergence can be obtained by considering an electron beam with uniform charge distribution within an elliptical cross-section [8], as shown in the inset of Fig. s6. The semi-major axis is X along the x direction, and the semi-minor axis is Y along the y direction. The electron beam is moving along the z direction with current I and velocity v. In the electron beam rest frame $x' - y' - z'$, the electrons are repelled by the electrostatic force, which can be derived from the electrostatic potential

$$\Phi'(x',y') = -\frac{\rho'}{2\varepsilon_0}\left(\frac{x'^2 Y + y'^2 X}{X+Y}\right), \tag{12}$$

where ρ' is the charge density in the rest frame, ε_0 is the vacuum permittivity, $x' = x$ and $y' = y$ are the position inside the electron beam. The charge density in the rest frame is $\rho' = \rho/\gamma$, where γ is the Lorentz factor and $|\rho| = I/(\pi XYv)$.

The electron beam axes evolve in the rest frame due to the electrostatic force

$$\frac{\mathrm{d}^2 X}{\mathrm{d}t'^2} = \frac{\mathrm{d}^2 Y}{\mathrm{d}t'^2} = \frac{e\rho'}{m\varepsilon_0}\left(\frac{XY}{X+Y}\right), \tag{13}$$

where m is the rest mass of an electron. With the approximation that the electron beam's longitudinal velocity remaining unchanged, $dt' = dz/(v\gamma)$, where z is the propagation distance of the electron beam in the lab frame. Therefore, we have

$$\frac{\mathrm{d}^2X}{\mathrm{d}z^2} = \frac{\mathrm{d}^2Y}{\mathrm{d}z^2} = \frac{2C}{X+Y} \tag{14}$$

where $C = \frac{1}{m\gamma^3 v^3} \frac{eI}{2\pi\varepsilon_0}$. The solutions to the above equations are

$$z = \frac{(X_0+Y_0)}{\sqrt{2C}} \frac{\sqrt{\pi}}{2} \mathrm{Erfi}\left[\sqrt{\ln \frac{X+Y}{X_0+Y_0}}\right] \tag{15}$$
$$X = Y + X_0 - Y_0,$$

with $z = 0$ being the point of zero beam divergence, which means $X(z=0) = X_0$, $Y(z=0) = Y_0$, and $\frac{dX}{dz} = \frac{dY}{dz} = 0$ when $z = 0$. The beam divergence angle is defined as

$$\theta = \mathrm{atan}\left(\frac{\mathrm{d}X}{\mathrm{d}z}\right) = \mathrm{atan}\left(\sqrt{2C \ln \frac{X+Y}{X_0+Y_0}}\right). \tag{16}$$

The above calculations show that the divergence is tied by the current and the electron energy, as demonstrated by the exemplary results in Fig. s7. The initial beam is considered collimated with a circular cross section of diameter $2X_0 = 2Y_0 = 30$ nm. The results show that both the divergence angles and the transverse shifts are negligible within hundreds nm propagation distance under the chosen parameters.

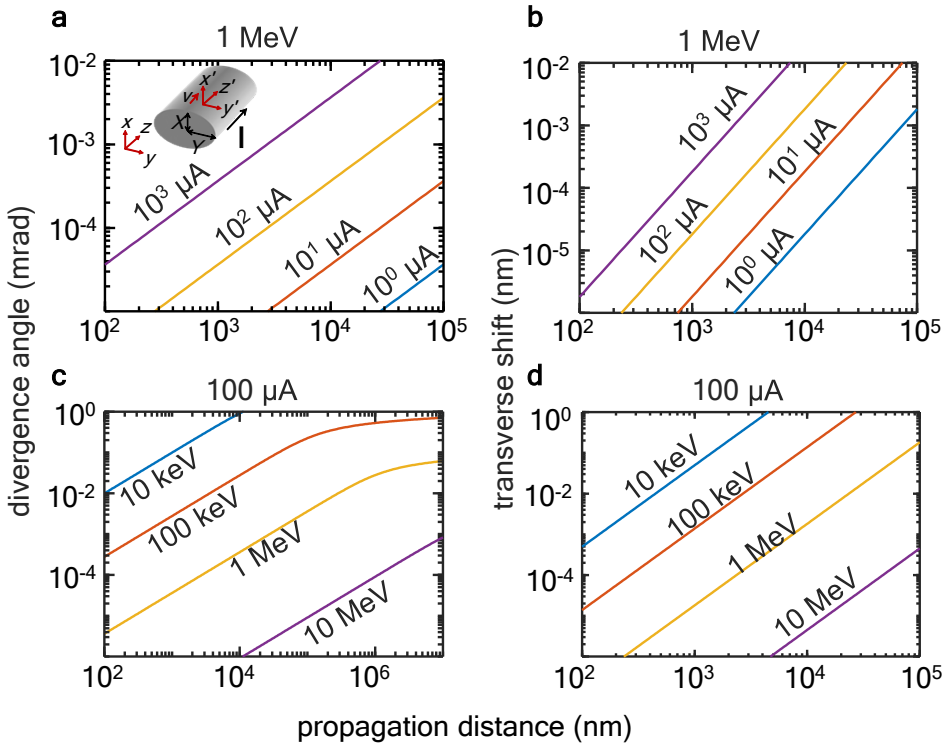

Fig. s7. Divergence of circular electron beams induced by space charge. (a,b) The electron energy is set to be 1 MeV. (c,d) The current is set to be 100 μA. The initial beam width at the focal plane is chosen as $2X_0 = 2Y_0 = 30$ nm for all the panels.

Next, we investigate the electron beam divergence induced by multiple scattering. Most of the deflection is due to Coulomb scattering from nuclei as described by the Rutherford cross section [9]. The rms divergence angle (θ^{rms}) and the transverse shift (T^{rms}) are described by

$$\theta^{\mathrm{rms}} = \sqrt{2}\frac{13.6\ \mathrm{MeV}}{\beta cp}\sqrt{\frac{z}{L_{\mathrm{R}}}}\left(1 + 0.038\ln\left(\frac{z^2}{L_{\mathrm{R}}\beta^2}\right)\right).$$
$$T^{\mathrm{rms}} = \frac{1}{\sqrt{3}}z\theta^{\mathrm{rms}} \tag{17}$$

where p is the electron momentum, z is the propagation distance, and L_{R} is the radiation length in the medium. Exemplary results are plotted in Fig. s8, which show that faster electrons are more collimated with the same propagation distance.

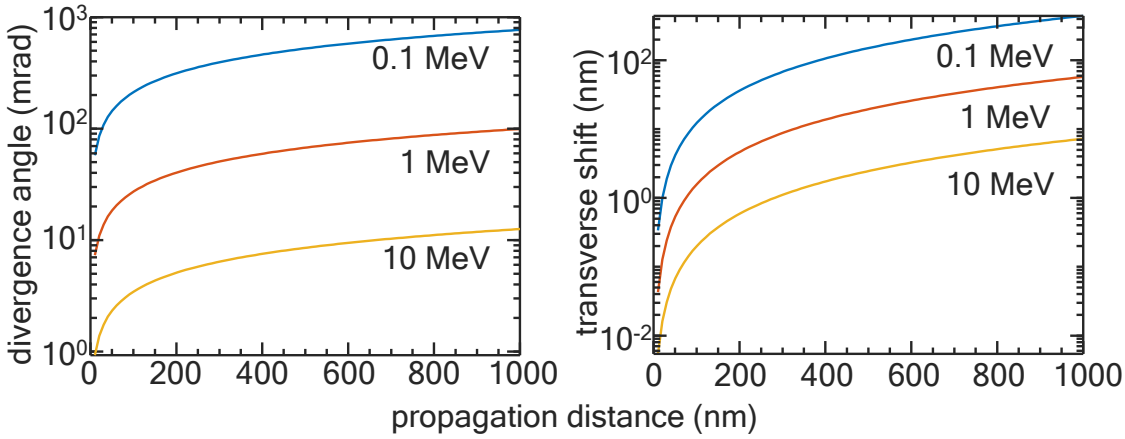

Fig. s8. Divergence of electron beams induced by electron multiple elastic scattering. The electron kinematic energies are 0.1 MeV, 1 MeV and 10 MeV.

Section 8 | Azimuthal distribution of the Airy beam

In Figs. 2 and 4 of the main text, we show the caustic phenomenon in the 2D plane. However, the caustic phenomenon extends in the azimuthal direction. In Fig. s9, we demonstrate the azimuthal distribution of the focusing effect at the caustics. The focused X-ray beams maintain high intensity over a broad angular range from $-30°$ to $30°$.

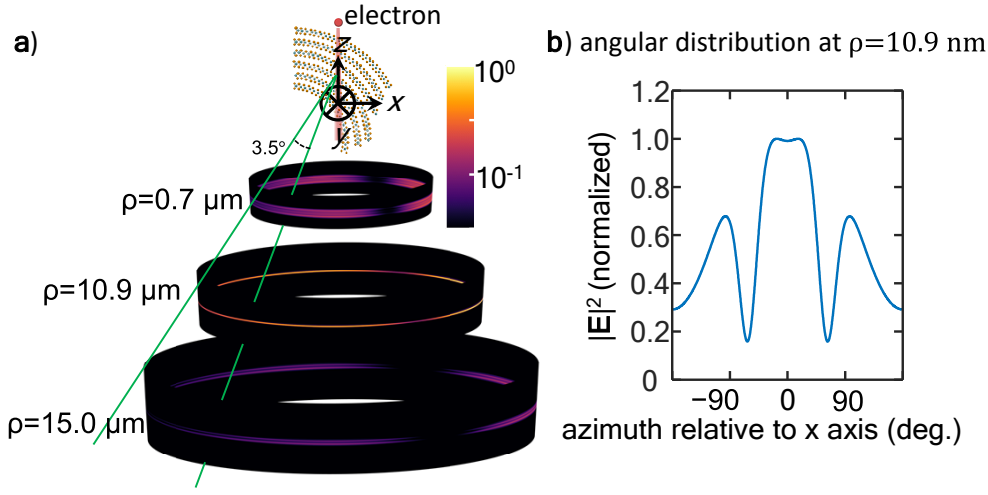

Fig. s9. Azimuthal distribution of the Airy beam. The setup is the same as used to generate Fig. 4b. **a**) shows the focusing effect of the caustics along the azimuthal direction. The intensity, however, is not radially symmetrical. **b**) plots the azimuthal distribution of the field intensity at caustics. The field distribution has a plateau over the angular range from $-30°$ to $30°$.

Section 9 | The photon flux of the Airy beam

The total energy traversing one infinitesimal patch $\boldsymbol{\sigma} = \sigma\hat{n}$ (small enough within which the flux is uniformly distributed) is

$$\Delta E = \int_{-\infty}^{\infty} dt(\mathbf{E}(\mathbf{r},t) \times \mathbf{H}(\mathbf{r},t)) \cdot \boldsymbol{\sigma}$$
$$= \int_{0}^{\infty} d\omega\hbar\omega \left[\frac{2\mathrm{Re}(\mathbf{E}(\mathbf{r},\omega) \times \mathbf{H}^*(\mathbf{r},\omega)) \cdot \hat{n}}{2\pi\hbar\omega}\right]\sigma, \quad (18)$$

where $\left[\frac{2\mathrm{Re}(\mathbf{E}(\mathbf{r},\omega) \times \mathbf{H}^*(\mathbf{r},\omega)) \cdot \hat{n}}{2\pi\hbar\omega}\right]\sigma$ is the number of photons traversing the patch $\boldsymbol{\sigma}$ per angular frequency per electron. Therefore, the photon flux density along the $\hat{n}$ direction is

$$\frac{2\mathrm{Re}(\mathbf{E}(\mathbf{r},\omega) \times \mathbf{H}^*(\mathbf{r},\omega)) \cdot \hat{n}}{2\pi\hbar\omega} \cdot \left|\frac{\mathrm{I}}{e}\right| \quad (19)$$

where I is the current.

In the following, we calculate the photon flux density of an Airy beam from an electron beam with 100 μA current and 1 MeV kinetic energy per electron. The diameter of the electron beam is 30 nm at the focal plane. The multiple electron scattering (Fig. s7) accounts for the electron beam divergence, while the space charge effect is negligible over a propagation distance of 300 nm. We use a Gaussian electron beam with a rms divergence angle $\delta\theta = 25$ mrad (average of the rms divergence angles for 1 MeV electrons along the 300 nm trajectory) and a rms spot size $\delta r = 19$ nm (average of the rms spot sizes of 1 MeV electrons along the 300 nm trajectory). The photon flux density at the plane $\rho = 10.9$ μm in Fig. 4b is shown in Fig. s10.

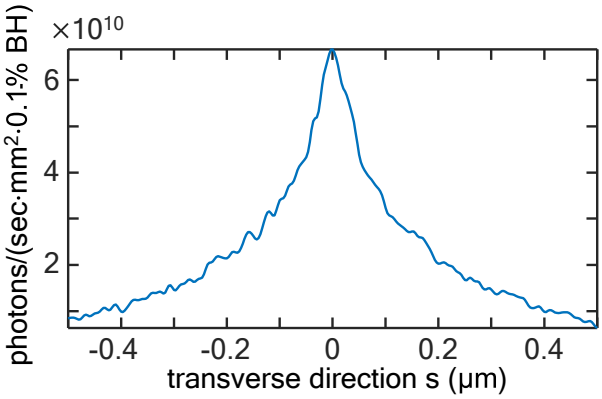

Fig. s10. The flux density at the central position of the Airy beam in Fig. 4b from a Gaussian electron beam. The details are listed in the content.

The total X-ray photon flux of the Airy beam can be calculated by combining the photon flux transverse density distribution in Fig. s10 and the azimuthal intensity distribution in Fig. s9. The cross-size area of the Airy beam is 2 μ m^2 at ρ=10.9 μm. Therefore, the total X-ray photon flux is 1.4×10^5 photons/(sec · 0.1% BH), corresponding to 2.3×10^{-10} photons/(electron · 0.1% BH).

Section 10 | Experimental design of characterizing the X-ray Airy beam

X-ray Airy beams can be characterized by the knife-edge scanning techniques [10,11]. A micron-sized pinhole or slot is used to both isolate the monochromatic Airy beam and block the secondary and large-angle scattered electrons. A

Pb or Rh analyzer with a cross section of 5 nm × 5 μm and 5 nm thick film is scanned by a nano positioning stage in the $x-y$ plane through the Airy beam with 2 nm reproducibility [12]. Silver L_α and L_β fluorescence lines are detected by the energy-dispersive spectroscopy (EDS), and scattered X-rays are collected by a scintillation counter (SC). Both EDS and SC are capable of charactering the X-ray Airy beam [12].

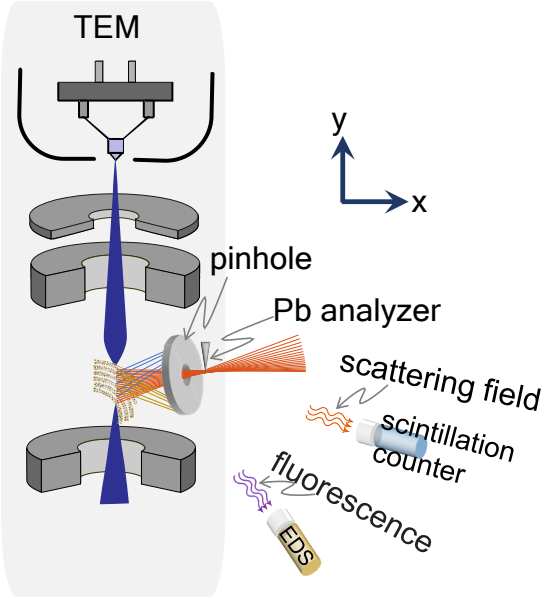

Fig. s11. Experimental design of characterizing the X-ray Airy beam in a TEM. The details of the setup are discussed in the content.

Section 11 | Photon density operator

The reduced density operator of the photons is $\rho_{\text{ph}} = \text{Tr}_{\text{ele}}(|f\rangle\langle f|)$, which is constructed from the final states of the joint system $|f\rangle = \sum_{\mathbf{p}',\mathbf{k}} \frac{1}{\sqrt{V}} \psi(\mathbf{k},\mathbf{p}')|\mathbf{p}'\rangle \otimes |1_{\mathbf{k}}\rangle$. We can also write ρ_{ph} as

$$\rho_{\text{ph}} = \frac{1}{V} \sum_{\mathbf{p}'} \sum_{\mathbf{k},\mathbf{k}'} \psi(\mathbf{k},\mathbf{p}')\psi^*(\mathbf{k}',\mathbf{p}')|1_{\mathbf{k}}\rangle \langle 1_{\mathbf{k}'}| \,. \tag{20}$$

Section 12 | Quantum aspects of the generation of X-ray caustics

For regular periodic crystals, the vector potential modes are written from Bloch's theorem as [13]

$$\mathbf{A}(\mathbf{r}) = \sum_{\{\text{n}\},\mathbf{k}} \mathbf{A}_{\mathbf{g},\mathbf{k}} e^{i(\mathbf{k}+\mathbf{g})\cdot\mathbf{r}} + c.c. = \sum_{\{\text{n}\},\mathbf{k}} \mathbf{u}_{\mathbf{g},\mathbf{k}} e^{i(\mathbf{k}+\mathbf{g})\cdot\mathbf{r}} a_{\mathbf{k}} + \text{c.c.}, \tag{21}$$

where the $\{\text{n}\}$ sum runs over the reciprocal lattices. The crystal structure of a bent vdW material is aperiodic because the crystal lattice rotates gradually along the electron trajectory, as shown in Fig. 1b of the main text. Therefore, the amplitude $\mathbf{u}_{\mathbf{g},\mathbf{k}}(\mathbf{r})$ and the reciprocal lattice vector $\mathbf{g}(\mathbf{r})$ are not constant but position dependent.

The initial electron-photon state is described as $|i\rangle = \sum_{\mathbf{p}} \frac{1}{\sqrt{V}} \psi(\mathbf{p})|\mathbf{p}\rangle \otimes |0\rangle$, where $\sum_{\mathbf{p}} \frac{1}{\sqrt{V}} \psi(\mathbf{p})|\mathbf{p}\rangle$ is the superposition of electron momentum states $|\mathbf{p}\rangle$ and $|0\rangle$ is the photon vacuum state. The final electron-photon state is $|f\rangle = \sum_{\mathbf{p}',\mathbf{k}} \frac{1}{\sqrt{V}} \psi(\mathbf{k},\mathbf{p}')|\mathbf{p}'\rangle \otimes |1_{\mathbf{k}}\rangle$. From Eq. (20), we know that the interference of different photon states relies on the overlap of the spectral function $\psi(\mathbf{k},\mathbf{p}')$. From the perturbation theory of quantum electrodynamics (QED),

$$\psi(\mathbf{k},\mathbf{p}') = -\frac{i}{\hbar}\int_0^t dt_1 \sum_{\mathbf{p}} \psi(\mathbf{p}) \left\langle 1_{\mathbf{k}}, \mathbf{p}' \right| e^{\frac{i}{\hbar}H_0^{(s)}t_1} \left\{ -\frac{q}{m}\mathbf{P}\cdot\mathbf{A}(\mathbf{r}) \right\} e^{-\frac{i}{\hbar}H_0^{(s)}t_1} \left| 0,\mathbf{p} \right\rangle \tag{22}$$

To evaluate the above equation, we proceed as follows:

$$\left\langle 1_{\mathbf{k}}, \mathbf{p}' \right| e^{\frac{i}{\hbar}H_0^{(s)}t_1} \left\{ -\frac{q}{m}\mathbf{P}\cdot\mathbf{A}(\mathbf{r}) \right\} e^{-\frac{i}{\hbar}H_0^{(s)}t_1} \left| 0,\mathbf{p} \right\rangle = \sum_{\{\mathrm{n}\}} \left\langle \mathbf{p}' \right| -\frac{q}{m}\mathbf{P}\cdot\mathbf{u}_{\mathbf{g},\mathbf{k}} e^{i(\mathbf{k}+\mathbf{g})\cdot\mathbf{r}} \left| \mathbf{p} \right\rangle e^{\frac{i}{\hbar}\left(-E_p+E_{p'}+\hbar\omega_k\right)t_1},$$

where $E_{p'}$, E_p, and $\hbar\omega_k$ are the energies of the electron final state, the electron initial state, and the emitted photon, respectively. The evaluation of $\left\langle \mathbf{p}' \right| -\frac{q}{m}\mathbf{P}\cdot\mathbf{u}_{\mathbf{g},\mathbf{k}} e^{i(\mathbf{k}+\mathbf{g})\cdot\mathbf{r}} \left| \mathbf{p} \right\rangle$ cannot be carried out analytically because both $\mathbf{u}_{\mathbf{g},\mathbf{k}}$ and $\mathbf{g}$ are position dependent for aperiodic crystals. We denote it as the transition matrix element $\mathcal{M}_{kpp'}$. Then Eq. (16) becomes

$$\begin{aligned} \psi(\mathbf{k},\mathbf{p}') &= -\frac{i}{\hbar}\sum_{\mathbf{p},\{\mathrm{n}\}} \psi(\mathbf{p}) \left\langle \mathbf{p}' \right| -\frac{q}{m}\mathbf{P}\cdot\mathbf{u}_{\mathbf{g},\mathbf{k}} e^{i(\mathbf{k}+\mathbf{g})\cdot\mathbf{r}} \left| \mathbf{p} \right\rangle \\ \int_0^t dt_1 e^{\frac{i}{\hbar}\left(-E_p+E_{p'}+\hbar\omega_k\right)t_1} &= -\frac{i}{\hbar}\sum_{\mathbf{p},\{\mathrm{n}\}} \psi(\mathbf{p}) \mathcal{M}_{kpp'} T\delta_{E_{p'}+\hbar\omega_k, E_p} \end{aligned} \tag{23}$$

where the energy conservation equation $T\delta_{E_{p'}+\hbar\omega_k, E_p} = \int_0^t e^{\frac{i}{\hbar}\left(-E_p+E_{p'}+\hbar\omega_k\right)t_1} dt_1$ is applied and T is the interaction time.

Section 13 | The robustness of the X-ray caustic against the electron energy distribution

In the main text, the electron energy is fixed at 1 MeV. However, there is a finite energy distribution for a practical electron beam. In Fig. s12, we compare the beam widths of the Airy beam and the collimated beam excited by the electron beam with Gaussian energy distributions. It shows that with small energy distribution widths, such as a standard deviation of less than 10 keV, the Airy beams are superior to the collimated beams in terms of intensity and beam width.

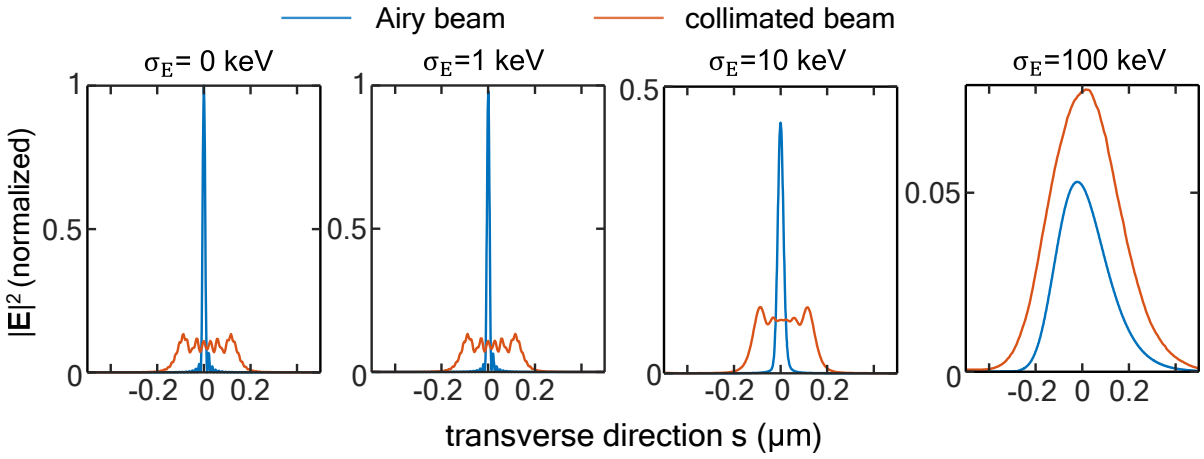

Figure s12. The effect of the electron energy distribution on the quality of the X-ray caustics. We test the robustness of the X-ray caustic concept by studying its dependence on electron beams with various Gaussian energy distributions. The mean of the distribution is 1 MeV, and the standard deviation is σ_E. The beam width is calculated at ρ =11.3 μm, with the same setup as used in Fig. 5c.

Semi-relativistic electrons (60 keV – 300 keV) can be found in transmission electron microscopes (TEMs), whereas modestly relativistic electrons (500 keV-5 MeV) are available in room-sized high-voltage transmission electron microscopes (HVTEMs) [14], in which a series of radio-frequency (RF) cavities are used. Highly relativistic electrons (5 MeV-10 MeV) require room-sized linear electron accelerators.

Section 14 | Comparison of state-of-the-art X-ray shaping paradigms

In Table s1, we compare the performance of different X-ray shaping paradigms. The cumbersome paradigms show good performances in terms of focal length and spot size, but require coherent X-rays which are achievable in large facilities such as free electron lasers. The compact schemes suffer from large spot sizes, due to the incoherent nature of the X-ray sources. The parameters of our bending vdW lens listed in the table represent typical results discussed in the main text, incorporating the electron beam divergence inside the crystal.

Table s1| State-of-the-art X-ray shaping paradigms

	cumbersome schemes				**compact schemes**	
	reflection mirror	zone-plate (diffraction)	refractive lens	tapered waveguide	polycapillary lens with an x-ray tube	our bending vdW lens
focal length	75 mm	4.2 mm	80-800 mm	4.9 mm	~3 mm	~10 μm
numerical aperture	0.004	0.005	10^{-4}-10^{-3}	10^{-4}	0.17	0.015-0.030
spot size	7 nm	11 nm	~10s μm	~ 10 nm	11-14 μm	100 nm
coherent focusing?	Yes	Yes	Yes	Yes	No	Yes
representative reference	Nat. Phys. 6, 122–125 (2010)	Sci. Rep. 3, 3562 (2013)	Nucl. Instrum. Meth. A 916, 275–282 (2019)	PRL 91, 204801 (2003)	Lindqvist, M. Thesis, Uppsala University, 2017	this work

References

[1] E. Shahmoon et al., "Cooperative Resonances in Light Scattering from Two-Dimensional Atomic Arrays," Phys. Rev. Lett. **118**, 113601 (2017).

[2] F. J. García de Abajo, "Optical excitations in electron microscopy," Rev. Mod. Phys. **82**, 209–275 (2010).

[3] C. T. Chantler, "Theoretical Form Factor, Attenuation, and Scattering Tabulation for Z=1–92 from E=1–10 eV to E=0.4–1.0 MeV," J. Phys. Chem. Ref. Data **24**, 71–643 (1995).

[4] P. V. Karataev, "Pre-wave zone effect in transition and diffraction radiation: Problems and solutions," Phys. Lett. Sect. A Gen. At. Solid State Phys. **345**, 428–438 (2005).

[5] D. B. Zhang et al., "Bending ultrathin graphene at the margins of continuum mechanics," Phys. Rev. Lett. **106**, 255503 (2011).

[6] E. Han et al., "Ultrasoft slip-mediated bending in few-layer graphene," Nat. Mater. **19**, 305–309 (2020).

[7] G. Wang et al., "Bending of Multilayer van der Waals Materials," Phys. Rev. Lett. **123**, 116101 (2019).

[8] F. J. Sacherer, "RMS envelope equation with space charge," IEEE Trans. Nucl. Sci. **18**, 1105–1107 (1971).

[9] P. A. Zyla et al., "Review of particle physics," Prog. Theor. Exp. Phys. **2020**, 083C01 (2020).

[10] A. H. Firester et al., "Knife-edge scanning measurements of subwavelength focused light beams," Appl. Opt. **16**, 1971–1974 (1977).

[11] M. Lindqvist, "Polycapillary X-Ray Optics for Liquid-Metal-Jet X-Ray Tubes," Thesis, Uppsala University (2017).

[12] H. C. Kang et al., "Focusing of hard x-rays to 16 nanometers with a multilayer Laue lens," Appl. Phys. Lett. **92**, 221114 (2008).

[13] H. Nitta, "Kinematical theory of parametric X-ray radiation," Phys. Lett. A **158**, 270–274 (1991).

[14] T. Sannomiya et al., "Transmission Electron Microscope Using a Linear Accelerator," Phys. Rev. Lett. **123**, 150801 (2019).